



저작자표시-비영리-변경금지 2.0 대한민국

이용자는 아래의 조건을 따르는 경우에 한하여 자유롭게

- 이 저작물을 복제, 배포, 전송, 전시, 공연 및 방송할 수 있습니다.

다음과 같은 조건을 따라야 합니다:



저작자표시. 귀하는 원저작자를 표시하여야 합니다.



비영리. 귀하는 이 저작물을 영리 목적으로 이용할 수 없습니다.



변경금지. 귀하는 이 저작물을 개작, 변형 또는 가공할 수 없습니다.

- 귀하는, 이 저작물의 재이용이나 배포의 경우, 이 저작물에 적용된 이용허락조건을 명확하게 나타내어야 합니다.
- 저작권자로부터 별도의 허가를 받으면 이러한 조건들은 적용되지 않습니다.

저작권법에 따른 이용자의 권리는 위의 내용에 의하여 영향을 받지 않습니다.

이것은 [이용허락규약\(Legal Code\)](#)을 이해하기 쉽게 요약한 것입니다.

[Disclaimer](#)

이학석사 학위논문

Interferometric Scattering Spectromicroscopy of Plasmonic Nanoparticles

간섭계 기반 산란 분광 현미경을 이용한
플라즈모닉 나노입자의 연구

2018년 8월

서울대학교 대학원
화학부 물리화학전공
이 한 결

Abstract

Interferometric scattering microscopy (iSCAT) is a powerful technique that enables label-free, real-time, and highly sensitive detection of a single scatterer like metal nanoparticle or small protein molecule. However, spectroscopic studies using iSCAT have been rarely performed because it is hard to separately interpret the intensity and phase information from iSCAT signal.

In this work, we newly developed new spectromicroscopy technique using iSCAT with tunable laser light source. By analyzing Gouy-phase shift, we successfully recovered the full localized surface plasmon resonance (LSPR) spectra from the iSCAT signal of the single gold nanoparticle (AuNP). Finite difference time domain (FDTD) simulation was performed to verify our experimental data.

Keyword : interferometric scattering microscopy, single particle spectroscopy, plasmonics, Gouy-phase shift

Student Number : 2016-26731

Table of Contents

Abstract	i
Table of Figures	iv
1. Introduction	1
1.1. Single Particle Spectroscopy	1
1.2. Interferometric Scattering Microscopy	2
1.3. Gouy–Phase Shift	6
1.4. Gouy–Phase Shift at the iSCAT	8
2. Experimental Section.....	10
2.1. Sample Preparation.....	10
2.2. Acquiring iSCAT Image Sets	12
2.3. Image Processing.....	14
3. Result and Discussion.....	16
4. Conclusion	27

5. Supplementary Information	28
5.1. iSCAT Spectromicroscope System	28
5.2. Finite Difference Time Domain Simulation	29
References.....	30
Abstract (in Korean)	33
Acknowledgement.....	34

Table of Figures

FIG 1. Schematic illustration of iSCAT system.....	3
FIG 2. Gaussian beam radius (green) and its Gouy-phase shift (red). The phase varies π rad around the beam waist.	6
FIG 3. Wide-field iSCAT image of spin-coated (randomly dispersed) 200 nm AuNPs	11
FIG 4. iSCAT image stacks with varying λ and z , significant contrast change was observed	13
FIG 5. (a) wide field iSCAT image of 78nm AuNP sample (b) raw scattering signal (c) background (d) normalized iSCAT images and (e) PSF fitting result of (d)	15
FIG. 6. (a) Experimental setup. SC, super-continuum laser; AOTF, acousto-optic tunable filter; BS, beam-splitter; BFP, back-focal plane; O, objective lens; PZT, piezoelectric z -scanner; S, sample surface; L_1 , a lens for defocused illumination; L_2 , tube-lens for imaging. (b) Zoom-in view of the scattering at sample surface: incident laser field (E_0) induces both the scattered field (E_{scat}) from a nanoparticle and the field reflected from air-substrate interface (E_{refl}). (c) The two field components acquire the Gouy-phase shift ($\Phi_{Gouy}(z)$) in the image plane, which changes with the vertical position (z) of the camera and / or the objective lens, yielding z -	

dependent iSCAT image contrasts. 16

FIG. 7. Vertical (z) focus dependent image contrast of AuNP scattering at $\lambda = 526 \text{ nm}$. (a)–(d) Experimental normalized iSCAT images and line–profiles of an AuNP at $\delta z = -520 \text{ nm}$, -195 nm , $+195 \text{ nm}$, $+520 \text{ nm}$. (e)–(h) Corresponding fitted iSCAT images and line profiles. Inset numbers denote the amplitude, A (see eqn. (22) and (23)) extracted from the fit. (i) The amplitude $A(z)$ plotted as a function of z –positions (filled circles), along with a fit to eqn. (23), yielding amplitude ($|s_n|$) and phase (ϕ_{scat}) of the AuNP scattering. Also shown in open circles are the maximum (A_{max}), minimum (A_{min}) of $A(\delta z)$, and the z –position of zero–crossing (δz_0). 22

FIG. 8. (a) Color–coded image plot of $A(\lambda, z)$ of a 78 nm AuNP. (b) iSCAT–recovered scattering intensity (red) and phase (blue) spectra extracted from (a). The spectrum in grey is the iSCAT amplitude spectrum obtained at a fixed $z = 0 \text{ nm}$ position. (b) Electrostatics simulation result of far–field scattering spectra of AuNP (78 nm in diameter). (d) & (e) Analogous experimental and simulated spectra for AuNP with 200 nm diameter. In (b)–(e), intensity spectra are normalized whereas the phase spectra are not rescaled. 24

1. Introduction

1.1. Single Particle Spectroscopy

Optical detection and spectroscopy of single nanoparticles (NPs) are becoming ever more essential tools with wide range of applications, from single cell biology to material science [1–8]. Single particle measurement is important because each individual particle has unique physical properties due to its heterogeneity of size, shape, and surface structure, all of which are not observable by ensemble measurement. For the detection of non-fluorescent NPs, dark-field scattering (DFS), in which unscattered light from the light source is spatially rejected, is widely used nowadays [9–11]. Because the scattering intensity scales with 6th-power of the diameter of NPs, DFS-detection of NPs becomes more difficult as the size of NPs decrease. The practical size-limit of detectable NPs by DFS is ~20 nm in diameter.

1.2. Interferometric Scattering Microscopy

Interferometric scattering microscopy (iSCAT) is one of the powerful technique to track a single nanoparticle or small protein molecule. [12–19] Label-free, high sensitivity, and real-time capability of iSCAT enables the real-time observation of supported lipid bilayer (SLB) formation [15] and detection of single protein molecule down to 15 kDa. [20,21]

Principles of iSCAT is described in FIG 1. When incident laser beam (with an electric field E_0) propagated on the sample, the Rayleigh scattering is occurred from the gold nanoparticle (AuNP) (E_{scat}) :

$$E_{scat} = \tilde{s}E_0 \quad (1)$$

, where $\tilde{s} = |\tilde{s}|e^{i\phi_{scat}}$ is a complex-numbered scalar function carrying information on amplitude ($|\tilde{s}|$) and phase-difference (ϕ_{scat}) between the driving field (E_0) and the scattered field.

At the same time, reference field (E_{refl}) is generated that is reflected from the top surface of the substrate (glass-air domain) :

$$E_{refl} = rE_0 \quad (2)$$

, where $r = |r|e^{i\phi_{refl}}$ is a function on reflection amplitude ($|r|$) and phase-difference (ϕ_{refl}).

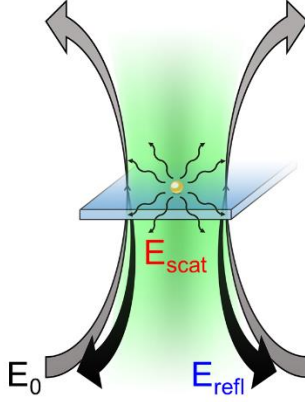


FIG 1. Schematic illustration of iSCAT system.

In this common-path interferometric system, self-interference between E_{scat} and E_{refl} is occurred and the intensity (I_{iSCAT}) is given by a scalar product of these two field components :

$$I_{iSCAT} = |E_{refl} + E_{scat}|^2 = |E_0|^2(|r|^2 + |\tilde{s}|^2 + 2|r||\tilde{s}| \cos \emptyset) \quad (3)$$

, where \emptyset is a phase-difference between E_{scat} and E_{refl} . In (3), pure scattering term $|\tilde{s}|^2$ is negligible because $|r|$ typically has

$10^3 \sim 10^4$ orders larger than $|\tilde{s}|$:

$$I_{iSCAT} \approx |E_0|^2 (|r|^2 + 2|r||\tilde{s}| \cos \emptyset) \quad (4)$$

, then we can acquire the E_{scat} signal amplified by 10^{3-4} orders using interferometry.

The magnitude of the iSCAT signal (approximately scales with $|E_{scat}||E_{refl}|$ that is 3rd-power of NPs diameter) is orders of magnitude larger than that of DFS signal ($|E_{scat}|^2$ scales with 6th-power of NPs diameter).

As can be seen above, I_{iSCAT} includes both intensity and phase information that are detected simultaneously. This can be an advantage to provide high spectral sensitivity because the phase largely varies around plasmonic resonance. However, one disadvantage is that iSCAT cannot directly provide separate amplitude ($|E_{scat}|$) and phase (ϕ_{scat}) of E_{scat} from single NP. This makes the iSCAT unusable for any quantitative analysis or spectroscopy, especially given that the ϕ_{scat} of NP is not known *a priori* and is highly dependent on the wavelength of light.

Furthermore, experimentally detected phase \emptyset has two components that are the phase from scattering of sample (ϕ_{scat}) and additional phase varying with laser propagation called Gouy-phase shift. (Φ_{Gouy}) [22,23] Because of such experimental difficulty,

spectroscopic studies using iSCAT have been performed before but have not been successful, such as poor interpretation of results [2] or confinement to theoretical calculations. [24]

1.3. Gouy–Phase Shift

When a Gaussian beam propagates through its beam waist (focus), it acquires additional phase shifts different from a plane wave which has same wavelength. Such difference is called Gouy–phase shift.

(see FIG 2) [22,23]

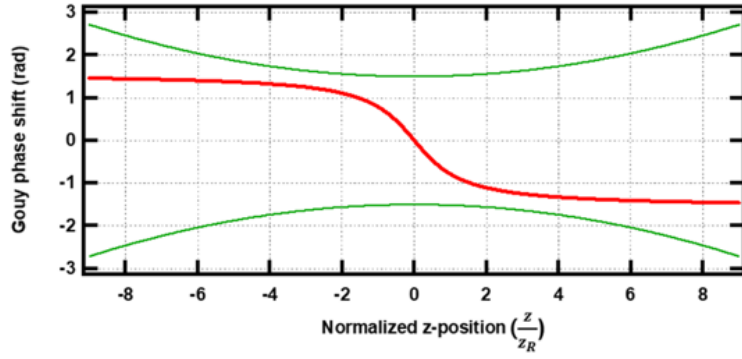


FIG 2. Gaussian beam radius (green) and its Gouy–phase shift (red).

The phase varies π rad around the beam waist.

Gouy–phase shift Φ_{Gouy} is given by :

$$\Phi_{Gouy} = -\tan^{-1} \frac{z}{z_R} \quad (5)$$

$$z_R = \frac{\pi w_0^2}{\lambda} \quad (6)$$

, when z_R is a Rayleigh length of the Gaussian beam and w_0 is

a beam waist radius.

From eqn. (5), (6), we can calculate the Gouy-phase shift by adjusting the relative z position between the beam waist and the AuNP.

1.4. Gouy–Phase Shift at the iSCAT

Back to eqn. (4), phase–difference between E_{scat} and E_{refl} , \emptyset can be written by eqn. (7–9) :

$$\emptyset = \phi_{refl} - \phi'_{scat} \quad (7)$$

$$\phi_{refl} = \theta_0 + \frac{\pi}{2} \quad (8)$$

$$\phi'_{scat} = \theta_0 - \Phi_{Gouy} - \phi_{scat} \quad (9)$$

, where θ_0 is the phase of E_0 , ϕ_{scat} is the phase retarded by NP that is an optical property of sample varying with wavelength. We know that ϕ_{refl} got $-\frac{\pi}{2}$ Gouy–phase shift because of the very long propagation length past the beam waist. Therefore, we can rearrange eqn. (7) as :

$$\emptyset = \Phi_{Gouy} + \theta_{scat} + \frac{\pi}{2} \quad (10)$$

, and put eqn. (10) into (4), rearrange the formula:

$$I_{iSCAT} = |E_0|^2 (|r|^2 - 2|r||\tilde{s}| \sin(\Phi_{Gouy} + \phi_{scat})) \quad (11)$$

, with subtracting $|r|^2$ term that is background signal, dividing $|E_0|^2$ for normalization, followed by neglecting $-2|r|$ that regards as constant with varying wavelength. Then we finally get :

$$I_{iSCAT}(\lambda, z) = |s(\lambda)| \sin(\Phi_{Gouy}(\delta z) + \phi_{scat}(\lambda)) \quad (12)$$

With a simple theoretical approach, we have determined that the signal we get from the iSCAT is a function of two variables (λ , δz) Furthermore, if we perform the experiment by adjusting λ and δz , we can expect to separate the intensity $|s(\lambda)|$ and phase $\phi_{scat}(\lambda)$ successfully.

2. Experimental Section

2.1. Sample Preparation

In iSCAT microscopy, a sample is typically prepared by drop-casting nanoparticle solution on glass coverslip and dried at room temperature. However, it is difficult to identify a single nanoparticle because of the formation of aggregates. So we used the spin-coating method to fabricate homogeneous nanoparticle monomers. Glass coverslip (24 × 60 mm, Marienfeld) was cleaned by sequential sonication for 5 min each in acetone, ethanol, distilled water. Then 20 μ L of gold nanoparticle solution (78nm synthesized from the Nam Lab. and 200nm purchased from BBI Solutions Inc.) was drop-casted on cleaned glass coverslip and spin-coated in 2 min at a rate of 500 rpm, followed by 0.5 min at 3000 rpm.

Numbers of homogeneous NP monomers were identified from fabricated samples subjected to wide-field iSCAT microscopy (see FIG 3).

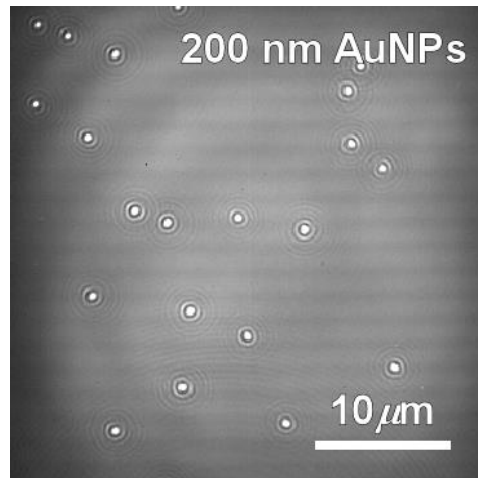


FIG 3. Wide-field iSCAT image of spin-coated (randomly dispersed) 200 nm AuNPs

2.2. Acquiring iSCAT Image Sets

As can be seen in eqn. (12), the scattering signal of AuNP in the iSCAT image (I_{iSCAT}) is a function of two variables which are wavelength λ and relative focus position δz . Therefore, it is necessary to obtain an image by adjusting both λ and δz .

During experiment, with the fixed δz , AOTF is used to scan the wavelength (450 - 800 nm). iSCAT image stacks were acquired simultaneously by CMOS camera with 2 ms of exposure time and 10 ms of frame time. Then, we adjusted δz using piezo-stage by 65 nm step, followed by wavelength scanning and image acquisition process. Independent repeated experiments were performed following procedures described above, and we finally obtained a complete image set containing spectral information of single AuNP. Also, the iSCAT image stacks of the background where no particles exist were obtained by moving the sample stage and scanning wavelength.

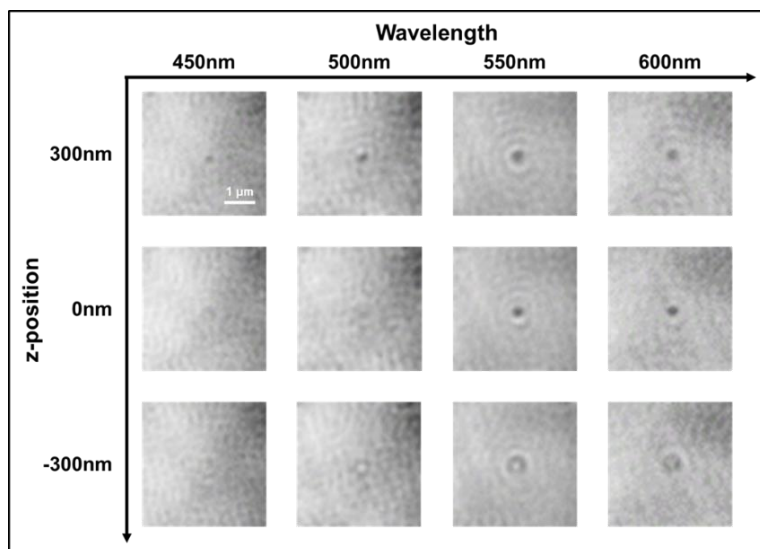


FIG 4. iSCAT image stacks with varying λ and z , significant contrast change was observed.

2.3. Image Processing

Our tunable laser light source using AOTF has different power varying by wavelength. Consequently, the CMOS camera responds differently depending on the wavelength because of its inherent quantum efficiency. Therefore, we must normalize the iSCAT images to extract the spectral information of AuNP.

Due to the experimental limitations, the background image stacks were acquired in only one δz position, but this was sufficient because the background images had negligible variance upon different δz position. We simply normalized background by subtracting background image (FIG 5(c) from raw image (FIG 5(b)).

It is almost impossible to manually process the whole image set more than 10 thousand images. Thus, the normalization process was computationally processed by programming with LabView.

After the normalization process, we should extract the spectral information of AuNP, which is implied in iSCAT image contrast largely varying with λ and δz . Also, particle on image slightly shifted during image acquisition process due to the experimental issues. In this case, introducing point spread function (PSF) made it easy to define the iSCAT image contrast and simultaneously track the particle.

We used the square root of a 2D airy disk model which is considered as more precise method compared to 2D Gaussian in processing the interferometric imaging [25] :

$$PSF_{iSCAT}(r) = A \frac{J_1(Br)}{Br} + C \quad (13)$$

$$J_1(Br) = \sum_{m=0}^{\infty} \frac{(-1)^m}{m!(m+1)!} \left(\frac{Br}{2}\right)^{2m+1} \quad (14)$$

$$r = \sqrt{(x - x_0)^2 + (y - y_0)^2} \quad (15)$$

, where $J_1(x)$ is the 1st order Bessel function of the 1st kind, A is amplitude, B is width, C is offset of the PSF. We defined the amplitude A as the iSCAT contrast, and we will call this observable as an iSCAT amplitude. Processed image using this model is shown in FIG 5(e).

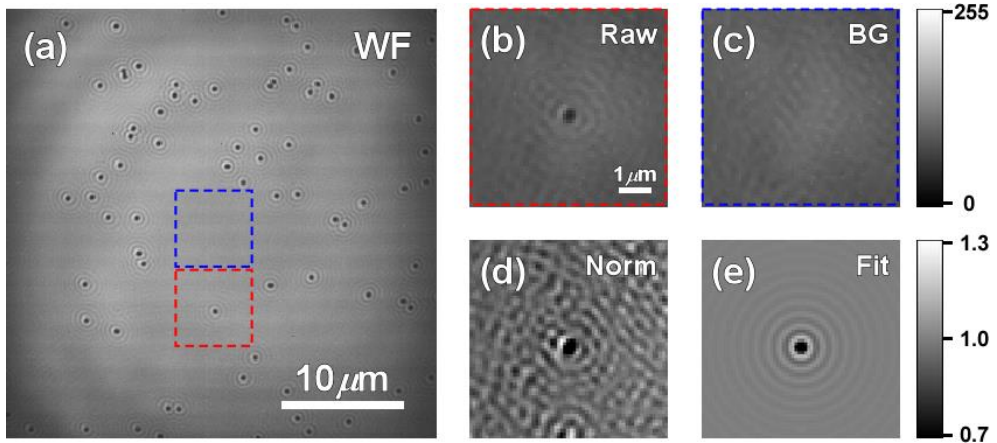


FIG 5. (a) wide field iSCAT image of 78nm AuNP sample (b) raw scattering signal (c) background (d) normalized iSCAT images and (e) PSF fitting result of (d)

3. Result and Discussion

As shown above, we recognized that a vertical (z)–scanning of microscope objective lens across the sample plane adds a z –dependent Gouy–phase shift between E_{scat} and E_{refl} , allowing us to recover the amplitude and phase of E_{scat} from a stack of z –specific iSCAT images of an NP. The method was validated by showing that the recovered amplitude and phase spectra of an AuNP fully reproduced the spectral features of localized dipole plasmon resonance of the AuNP.

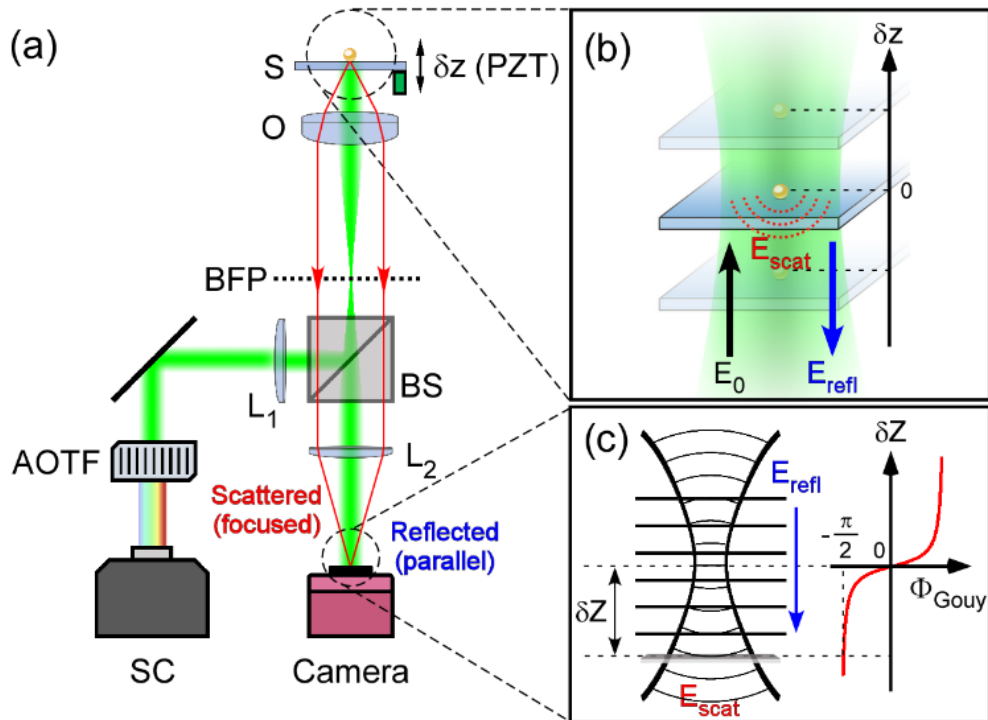


FIG. 6. (a) Experimental setup. SC, super-continuum laser; AOTF, acousto-optic tunable filter; BS, beam-splitter; BFP, back-focal plane; O, objective lens; PZT, piezoelectric z-scanner; S, sample surface; L_1 , a lens for defocused illumination; L_2 , tube-lens for imaging. (b) Zoom-in view of the scattering at sample surface: incident laser field (E_0) induces both the scattered field (E_{scat}) from a nanoparticle and the field reflected from air-substrate interface (E_{refl}). (c) The two field components acquire the Gouy-phase shift ($\Phi_{Gouy}(z)$) in the image plane, which changes with the vertical position (z) of the camera and / or the objective lens, yielding z -dependent iSCAT image contrasts.

FIG 6 is the experimental scheme employed in this study. A collimated super-continuum (SC, NKT photonics) laser output was filtered by an acousto-optic tunable filter (AOTF, Gooch&Housego) to obtain a quasi-monochromatic light (bandwidth of full-width at half maximum, FWHM 2 nm at 532 nm). The output light is focused onto the back-focal plane (BFP) of the objective lens (1.42NA) through a 50:50 neutral beam-splitter and a lens (L_1), to obtain wide-field illumination (with an electric-field of E_0) of the sample surface (illumination diameter of 15 μm). Samples were randomly dispersed AuNPs on a glass coverslip. Sample generated the field

that is reflected at the top surface of the substrate (\vec{E}_{refl}) and scattered by an AuNP ($\vec{E}_{scat}(\vec{r}_0, \vec{r})$). Coherent sum of the two field components was collected by the same objective lens and its intensity was projected onto the image-plane.

$$\vec{E}_{scat}(\vec{r}) = \tilde{s} \hat{e}_{scat}(\vec{r}) E_0 \quad (16)$$

, where $\hat{e}_{scat}(\vec{r})$ is a normalized scattering field pattern (basis) originating from a scatterer at $\vec{r}_0 = (0,0,0)$. The $\tilde{s} = |\tilde{s}|e^{i\phi_{scat}}$ is a complex-numbered scalar function carrying information on amplitude ($|\tilde{s}|$) and phase-difference (ϕ_{scat}) between the driving field (E_0) and the scattered field. The scattered field is focused (projected) onto the image plane at $Z = 0$ as below, (we ignored the polarizations on the imaged fields):

$$E'_{scat}(X, Y; Z = 0) = A\tilde{s} \left(\frac{J_1(BR)}{BR} \right) E_0 \quad (17)$$

, where $R = \sqrt{X^2 + Y^2}$ is the radial distance on image plane from the center of scatterer, $J_1(..)$ is the 1st order Bessel function of the first kind, and B is constant that determines the FWHM of focal area, and A is constant representing the collection efficiency of the microscope system as described above. When the objective lens

position was slightly detuned from its real focal position by δz , scattered field is focused on a Z -position displaced by $\delta Z = M \cdot \delta z$, where M , the magnification ratio, is the ratio of effective focal length (EFL) of the objective lens and the focal length of the tube lens (L_2). Slightly defocused field profile at detector position ($Z_d = 0$) is :

$$E'_{scat}(X, Y; Z = \delta Z) = A\tilde{s}e^{i\Phi_{Gouy}(\delta Z)} \left(1 + \left(\frac{\delta Z}{Z_R}\right)^2\right)^{-\frac{1}{2}} \left(\frac{J_1(B'R)}{B'R}\right) E_0 \quad (18)$$

, where Z_R is the Rayleigh length associated with the re-focusing of scattered field by a tube-lens (L_2). The $\Phi_{Gouy}(\delta Z)$ is the Gouy-phase shift [22,23] associated with the focusing of scattered field, which is defined as: $\Phi_{Gouy}(\delta Z) = -\tan^{-1}\left(\frac{\delta Z}{Z_R}\right)$. The eqn. (18) can be re-written in term of δz and $z_R = Z_R / M$:

$$E'_{scat}(X, Y; z = \delta z) = A\tilde{s}e^{i\Phi_{Gouy}(\delta z)} \left(1 + \left(\frac{\delta z}{z_R}\right)^2\right)^{-\frac{1}{2}} \left(\frac{J_1(B'R)}{B'R}\right) E_0 \quad (19)$$

As can be seen from eqn. (18) and (19), z -scanning of the objective lens across the focus results the scanning of the scattered field at the detector plane. The reflected field, on the other hand, is projected onto the detector plane as a plane wave (FIG 6(c)), and thus its amplitude and phase do not change significantly with z -

scanning of the objective lens :

$$E'_{refl}(X, Y; z = \delta z) = rE_0 \quad (20)$$

, where r is the Fresnel reflection coefficient of the air–glass substrate interface. For a visible wavelength range, the r is nearly constant. The field intensity profile on detector is:

$$\begin{aligned} I(X, Y; z = \delta z) &= \frac{|E'_{scat} + E'_{refl}|^2}{|E_0|^2} \\ &\cong |r|^2 - 2|r||\tilde{s}| \left(1 + \left(\frac{\delta z}{z_R}\right)^2\right)^{-\frac{1}{2}} \sin\left(\phi_{scat} + \tan^{-1}\left(\frac{\delta z}{z_R}\right)\right) \left(\frac{J_1(B'R)}{B'R}\right) \end{aligned} \quad (21)$$

In eqn. (21), we have neglected the smallest term, $|E_{scat}|^2$, and the proportionality constant A is included into $|\tilde{s}|$. The first term in eqn. (21) is a constant intensity offset (background) of the image, the $\left(\frac{J_1(B'R)}{B'R}\right)$ is the point spread function (PSF) of the image feature, and the factor in front of the PSF is the relative image contrast with respect to the intensity offset. Thus, background normalized iSCAT contrast, as defined as $I_n = (I(X, Y; z = \delta z) - |r|^2)/|r|^2$, has a form of :

$$\begin{aligned}
& I_n(X, Y; z = \delta z) \\
& \cong 2|\tilde{s}|/|r| \left(1 + \left(\frac{\delta z}{z_R}\right)^2\right)^{-\frac{1}{2}} \sin\left(\phi_{scat} + \tan^{-1}\left(\frac{\delta z}{z_R}\right)\right) \left(\frac{J_1(B'R)}{B'R}\right)
\end{aligned} \tag{22}$$

Thus, fitting of normalized iSCAT image to $A\left(\frac{J_1(B'R)}{B'R}\right)$ provide information on:

$$A(\delta z) = |\tilde{s}_n| \left(1 + \left(\frac{\delta z}{z_R}\right)^2\right)^{-\frac{1}{2}} \sin\left(\phi_{scat} + \tan^{-1}\left(\frac{\delta z}{z_R}\right)\right) \tag{23}$$

A set of $A(\delta z)$ for various δz thus can provide $|\tilde{s}|/|r|$ and ϕ_{scat} of an AuNP scattering.

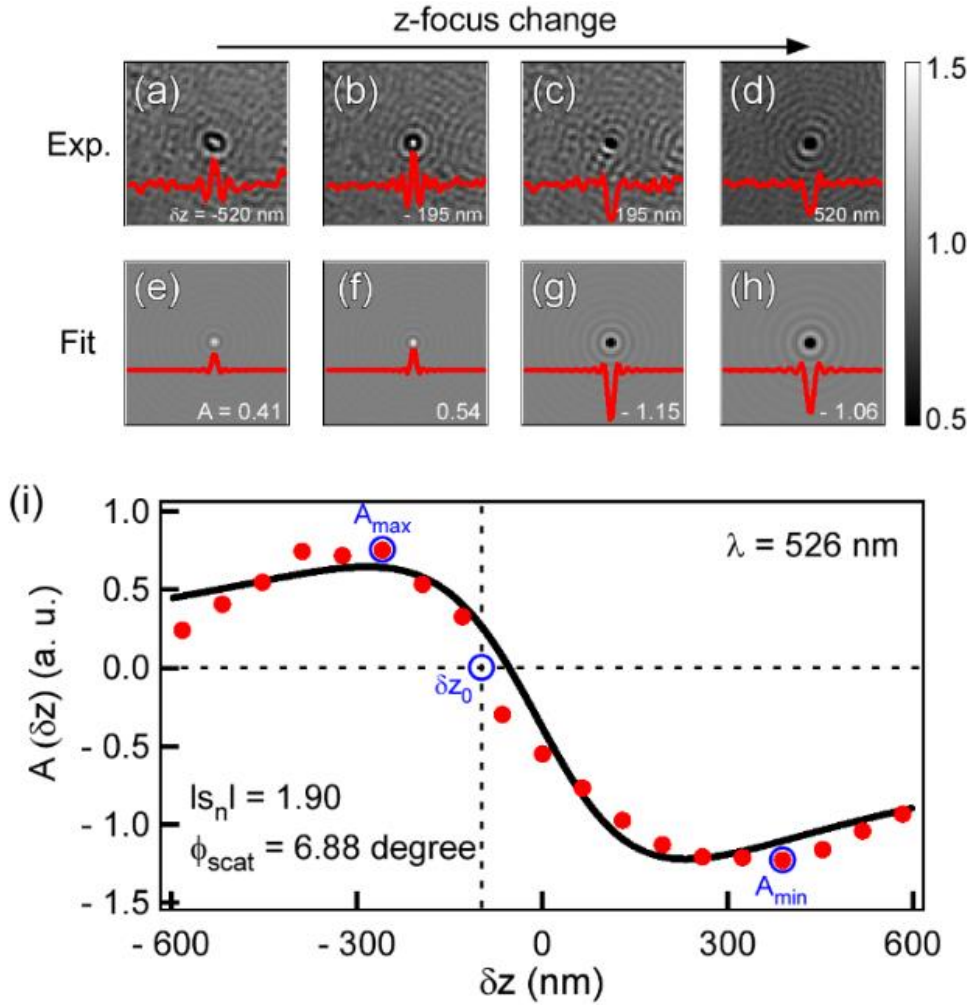


FIG. 7. Vertical (z) focus dependent image contrast of AuNP scattering at $\lambda = 526$ nm. (a)–(d) Experimental normalized iSCAT images and line-profiles of an AuNP at $\delta z = -520$ nm, -195 nm, $+195$ nm, $+520$ nm. (e)–(h) Corresponding fitted iSCAT images and line profiles. Inset numbers denote the amplitude, A (see eqn. (22) and (23)) extracted from the fit. (i) The amplitude $A(z)$ plotted as a function of z -positions (filled circles), along with a fit to eqn. (23), yielding amplitude ($|s_n|$) and phase (ϕ_{scat}) of the AuNP scattering.

Also shown in open circles are the maximum (A_{max}), minimum (A_{min}) of $A(\delta z)$, and the z -position of zero-crossing (δz_0).

FIG 7(a) (b) show the background-normalized iSCAT images of an AuNP (average diameter of 78 nm) obtained at the wavelength of $\lambda = 526$ nm, measured as a function of $\delta z = -520$ nm \sim + 520 nm, showing a clear contrast inversion caused by the Gouy-phase shift. FIG 7(c)–(h) are the corresponding fitted images, providing z -dependent iSCAT amplitude $A(\delta z)$ (values shown as inset). FIG 7(i) shows the plot of $A(\delta z)$ versus δz obtained by the procedure above. The plot was successfully fitted to eqn. (23) (black solid curve) to yield the amplitude $|s_n|$ and ϕ_{scat} of a AuNP scattering. Alternatively, the maximum amplitude (A_{max}), minimum amplitude (A_{min}), and zero-crossing δz values of the $A(\delta z)$ can be used to obtain approximate amplitude and phase ($|s_n(\lambda)| \propto A_{max} - A_{min}$ and $\phi(\lambda) \cong -\tan^{-1}\left(\frac{\delta z_0}{z_R}\right)$), where z_0 is the zero-crossing δz).

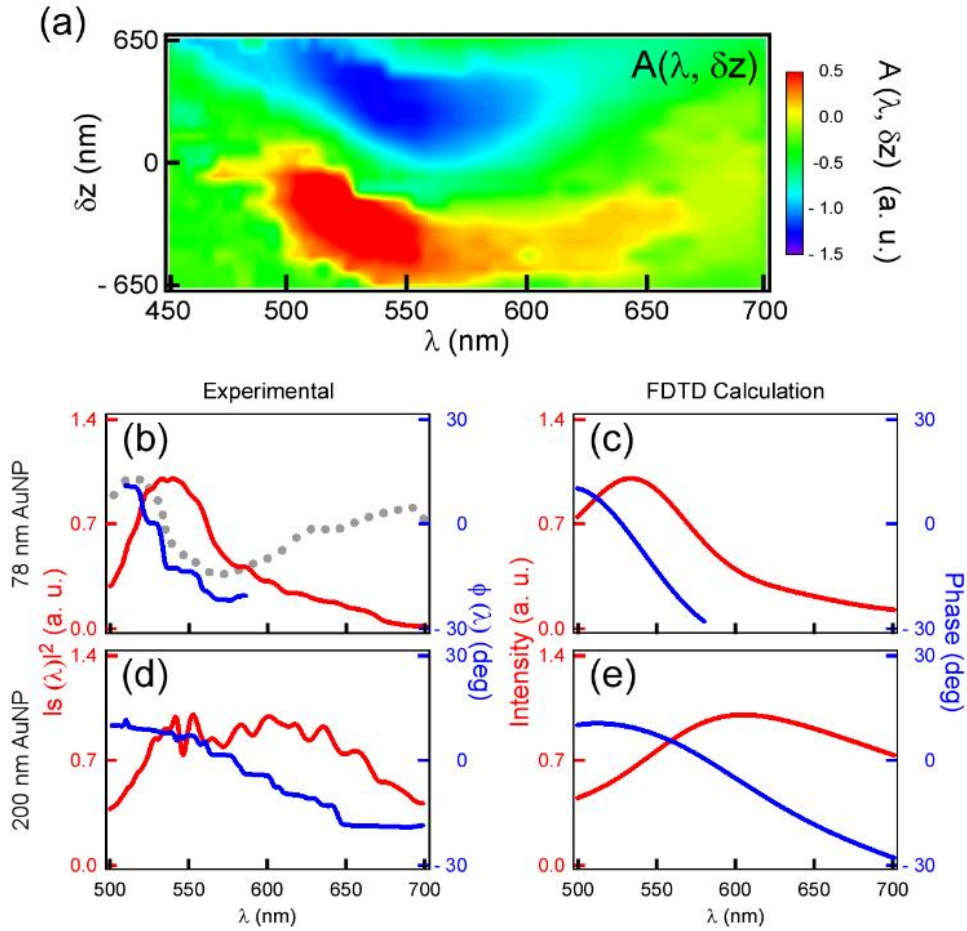


FIG. 8. (a) Color-coded image plot of $A(\lambda, z)$ of a 78 nm AuNP. (b) iSCAT-recovered scattering intensity (red) and phase (blue) spectra extracted from (a). The spectrum in grey is the iSCAT amplitude spectrum obtained at a fixed $z = 0$ nm position. (b) Electrodynamics simulation result of far-field scattering spectra of AuNP (78 nm in diameter). (d) & (e) Analogous experimental and simulated spectra for AuNP with 200 nm diameter. In (b)–(e), intensity spectra are normalized whereas the phase spectra are not rescaled.

To validate the procedure further, we have carried out spectroscopic iSCAT measurement on AuNP and compared it against well-known plasmon-resonance scattering spectra. FIG 8(a) displays the color-coded map of $A(\lambda, \delta\mathbf{z})$ of an AuNP obtained by analyzing the z -dependent normalized iSCAT images for a series of wavelengths $\lambda = 450 - 700$ nm. For each λ , $A(\lambda, \delta\mathbf{z})$ was fitted to eqn. (23) to obtain $|s_n(\lambda)|^2$ and $\phi_{scat}(\lambda)$, and the results for an AuNP (diameter of 78 nm) is plotted in FIG 8(b). The intensity spectrum shows a clear resonance at $\lambda_{res} = 526$ nm, corresponding to the dipolar plasmon resonance of AuNP. Corresponding phase spectrum showed rapid (~ 60 degree) phase variation across the λ_{res} , showing the correct phase variation of the driven oscillator across its resonance. Furthermore, both intensity and phase spectra showed a near quantitative match with numerically simulated (FIG 8(c), the finite-difference time-domain method) far-field scattering intensity and phase spectra of an AuNP. As a comparison, we plotted the iSCAT amplitude spectrum (gray curve) in FIG 8(b) obtained from a fixed z -position ($z = 0$ nm), showing the feature that does not correctly represent either the scattering intensity or phase spectra of an AuNP. FIG 8(d) (e) show another set of experimental iSCAT spectra and model spectra of larger AuNP (diameter of 200 nm), both showing that iSCAT spectra can also reproduce the peak broadening

and red-shift of the resonance with increasing with AuNP diameter. Overall match between iSCAT spectra and the model plasmon resonance spectra clearly confirms that the z-scanned iSCAT method correctly recover the AuNP scattering intensity and phase, and their spectra.

4. Conclusion

We developed the new spectromicroscopy technique that was not performed beforehand. This technique successfully enabled us to recover the full LSPR spectra including intensity and phase information of the single nanoparticle. FDTD simulation was carried out to verify our experimental spectra.

Current state-of-art detection limit of the iSCAT can reach the sensitivity sufficient for single-protein detection. As such, with an improved light source quality and with the full implementation of image filtering algorithm, our new technique, the z-scanning iSCAT should be able to provide scattering spectra of sub-10 nm NPs and also individual molecules.

5. Supplementary Information

5.1. iSCAT Spectromicroscope System

iSCAT spectromicroscope setup is similar to typical monochromatic iSCAT setup except for light sources. The output of a supercontinuum laser (Fianium SC-400-4, 400 - 2400nm) is directly input to acousto-optic tunable filter (AOTF, Gooch & Housego TF625-350-2-11-BR1A). Then output laser is spatially filtered using single mode optical fiber (Thorlabs, S405-XP) and adjusted to 1.5 mm of beam diameter. Output 450 - 700 nm tunable laser light is delivered to inverted microscope body (Olympus IX71) and focused at back focal plane (BFP) of an oil immersion objective lens (Olympus PLAPON 1.42 NA, 60 \times) to achieve wide-field illumination, with an achromatic doublet (Edmund optics, 150 mm focal length) after passing a 50:50 beam splitter. The polarization of incident beam is s-polarized and tuning with superachromatic half-wave plate. (Thorlabs SAHWP05M-700, 310 ~ 1100 nm) Then scattered and reflected light were focused with same objective lens and imaged onto CMOS camera (Photonfocus MV1-D1024E-160-CL-12) through magnifying tube lens included microscope body.

5.2. Finite Difference Time Domain Simulation

Theoretical calculation (Finite difference time domain (FDTD) simulation, *FDTD solutions*, Lumerical Inc.) was performed to verify whether the experimentally acquired spectra is reliable. The simulation was carried on the condition that total-field scattered-field linearly polarized light source (400 - 1000 nm) enters the AuNP (78 nm and 200 nm) which refractive index referred from Johnson and Christy [26], in vacuum and substrate was not considered. All calculations were carried with 0.5 nm mesh size.

References

- [1] D. Boyer, P. Tamarat, A. Maali, B. Lounis, and M. Orrit, *Science* **297**, 1160 (2002).
- [2] K. Lindfors, T. Kalkbrenner, P. Stoller, and V. Sandoghdar, *Phys. Rev. Lett.* **93**, 037401 (2004).
- [3] M. A. van Dijk, A. L. Tchebotareva, M. Orrit, M. Lippitz, S. Berciaud, D. Lasne, L. Cognet, and B. Lounis, *PCCP* **8**, 3486 (2006).
- [4] P. Kukura, M. Celebrano, A. Renn, and V. Sandoghdar, *Nano Lett.* **9**, 926 (2009).
- [5] A. Gaiduk, M. Yorulmaz, P. V. Ruijgrok, and M. Orrit, *Science* **330**, 353 (2010).
- [6] P. Kukura, M. Celebrano, A. Renn, and V. Sandoghdar, *The Journal of Physical Chemistry Letters* **1**, 3323 (2010).
- [7] M. Celebrano, P. Kukura, A. Renn, and V. Sandoghdar, *Nature Photonics* **5**, 95 (2011).
- [8] X. Hong, E. M. P. H. van Dijk, S. R. Hall, J. B. Götte, N. F. van Hulst, and H. Gersen, *Nano Lett.* **11**, 541 (2011).
- [9] S. Schultz, D. R. Smith, J. J. Mock, and D. A. Schultz, *Proceedings of the National Academy of Sciences* **97**, 996 (2000).
- [10] M. Hu, C. Novo, A. Funston, H. Wang, H. Staleva, S. Zou, P.

Mulvaney, Y. Xia, and G. V. Hartland, *J. Mater. Chem.* **18**, 1949 (2008).

[11] K. A. Willets, A. J. Wilson, V. Sundaresan, and P. B. Joshi, *Chem. Rev.* **117**, 7538 (2017).

[12] H. Ewers, V. Jacobsen, E. Klotzsch, A. E. Smith, A. Helenius, and V. Sandoghdar, *Nano Lett.* **7**, 2263 (2007).

[13] P. Kukura, H. Ewers, C. Müller, A. Renn, A. Helenius, and V. Sandoghdar, *Nature Methods* **6**, 923 (2009).

[14] J. Ortega–Arroyo and P. Kukura, *PCCP* **14**, 15625 (2012).

[15] J. Andrecka, K. M. Spillane, J. Ortega–Arroyo, and P. Kukura, *ACS Nano* **7**, 10662 (2013).

[16] C.–L. Hsieh, S. Spindler, J. Ehrig, and V. Sandoghdar, *The Journal of Physical Chemistry B* **118**, 1545 (2014).

[17] J. Ortega Arroyo, J. Andrecka, K. M. Spillane, N. Billington, Y. Takagi, J. R. Sellers, and P. Kukura, *Nano Lett.* **14**, 2065 (2014).

[18] M. Piliarik and V. Sandoghdar, *Nature Communications* **5**, 4495 (2014).

[19] J. O. Arroyo and P. Kukura, *Nature Photonics* **10**, 11 (2015).

[20] D. Cole, G. Young, A. Weigel, A. Sebesta, and P. Kukura, *ACS Photonics* **4**, 211 (2017).

[21] M. Liebel, J. T. Hugall, and N. F. van Hulst, *Nano Lett.* **17**, 1277 (2017).

- [22] C. R. Gouy, Acad. Sci. Paris **110**, 1251 (1890).
- [23] A. E. Siegman, *Lasers* (University Science, Mill Valley, CA,, (1986).
- [24] J. Hwang and W. E. Moerner, Opt. Commun. **280**, 487 (2007).
- [25] C.-Y. Cheng and C.-L. Hsieh, ACS Photonics **4**, 1730 (2017).
- [26] P. B. Johnson and R. W. Christy, Physical Review B **6**, 4370 (1972).

Abstract (in Korean)

간섭계 기반 산란 분광 현미경을 이용한 플라즈모닉 나노 입자의 연구

간섭계 기반 산란 현미경 (iSCAT)은 작은 금속 나노 입자 혹은 단백질 분자와 같은 단일 산란체의 고감도, 실시간, 라벨 없는 감지 및 영상화를 가능하게 하는 강력한 도구이다. 하지만 iSCAT을 이용한 분광학적 연구는 거의 수행되지 않았는데 이는 iSCAT 신호에서 세기와 위상을 분리하여 해석해 내기 어렵기 때문이다.

본 연구에서 우리는 iSCAT에 가변 레이저 광원을 접목하여 새로운 분광현미경 기법을 개발하였다. Gouy-위상 변화의 분석을 통해 단일 금 나노 입자의 iSCAT 신호로부터 국지화된 표면 플라즈몬 공명 스펙트럼을 성공적으로 복원해 낼 수 있었으며, 이러한 실험 결과의 타당성을 증명하기 위해 유한차분 시간영역 (FDTD) 이론 계산을 수행하였다.

Acknowledgement

부족한 제가 학위를 받기까지는 여러 사람들의 도움이 필요했습니다.

먼저 학위 과정동안 저를 지도해주신 김지환 교수님께 감사의 말씀을 드리고 싶습니다. 학문에 뜻이 없던 학부생 시절에 들은 교수님의 수업에서 처음으로 물리화학에 대한 관심을 가지게 되었고, 대학원에 진학해서는 즐겁게 연구할 수 있도록 지도해 주셨습니다. ‘본받고 싶다.’ 라는 말은 너무나 식상하지만, 그럼에도 불구하고 본받고 싶은 제 지도교수님께 다시 한 번 감사드립니다. 학위 과정을 밟으면서 훌륭한 교수님의 지도를 받았다는 것은 더할 나위 없는 커다란 행운이었으며, 이어 나갈 박사 과정에서도 이러한 행운이 이어지는 것에 또한 감사함을 느낍니다.

연구실 생활을 하며 만난 여러 학우들에게도 감사의 말씀을 올립니다. 처음 연구실에 입학했을 때부터 실험적, 이론적으로 많은 도움을 주었던 같은 팀의 정규일 형님, 최부건 학우, 다른 팀이지만 연구에 대해 같이 의견을 나누고, 제 일인 것처럼 시간을 들여 실험을 도와주셨던 구자정, 이강섭 형님, 이론 계산을 통해 본 연구에 직접적으로 도움을 주셨던 연구진, 박상민 형님, 과제를 함께 진행하며 나노 입자 합성과 시료 제작에 큰 도움을 주었던 남좌민 교수님 연구실의 김선기 학우에게 감사의 말씀을 전합니다. 연구에 있어 접점은 없었더라도 연구실 생활에 도움을 주셨던 다른 모든 연구실

선후배님들께도 감사드립니다. 대학원 생활 중 만난 한 분 한 분이
저에게는 모두 가르침을 주는 선생님이었습니다.

그리고 대학원 생활 중 힘든 일이 있을 때면 언제나 같이
고민해주며 힘을 주었던 친구들, 백인환, 조완상 군, 감사합니다.

마지막으로 가족들에게, 아버지, 어머니, 누나. 늘 제 선택을
존중해 주고 물심양면으로 응원해 주었기에 무사히 학위를 마칠 수
있었습니다. 고맙습니다. 사랑합니다.